

Ultrafast time-evolution of magnetic chirality probed by circular dichroism in x-ray resonant magnetic scattering in homochiral skyrmionic systems

Cyril Leveillé¹, Erick Burgos-Parra^{1,2}, Yanis Sassi², Fernando Ajejas², Valentin Chardonnet³, Emanuele Pedersoli⁴, Flavio Capotondi⁴, Giovanni De Nino^{4,5}, Francesco Maccherozzi⁶, Sarnjeet Dhesi⁶, David M. Burn⁶, Gerrit van der Laan⁶, Oliver S. Latcham⁷, Andrey V. Shytov⁷, Volodymyr V. Kruglyak⁷, Emmanuelle Jal³, Vincent Cros², Jean-Yves Chauleau⁸, Michel Virets⁸, Nicolas Reyren², and Nicolas Jaouen¹

¹*Synchrotron SOLEIL, Saint-Aubin, Boîte Postale 48, 91192 Gif-sur-Yvette Cedex, France*

²*Unité Mixte de Physique, CNRS, Thales, Univ. Paris-Saclay, 91767 Palaiseau, France*

³*Sorbonne Université, CNRS, LCPMR, 75005 Paris, France*

⁴*Elettra-Sincrotrone Trieste, 34149 Basovizza, Trieste, Italy*

⁵*University of Nova Gorica, 5000 Nova Gorica, Slovenia*

⁶*Diamond Light Source, Harwell Science and Innovation Campus, Didcot, Oxfordshire, OX11 0DE, UK*

⁷*University of Exeter, Stocker road, Exeter, EX4 4QL, United Kingdom.*

⁸*SPEC, CEA, CNRS, Université Paris-Saclay, 91191 Gif-sur-Yvette, France*

Abstract:

Noncollinear spin textures in ferromagnetic ultrathin films are attracting a renewed interest fuelled by the discovery of the interfacial Dzyaloshinskii-Moriya (DM) interaction. They are at the origin of complex chiral spin textures such as chiral magnetic domain walls, spin spirals, and magnetic skyrmions. We report here on the ultrafast behavior of chiral domain walls in perpendicularly magnetized asymmetric multilayers after optical pumping probed using circular dichroism in time-resolved x-ray resonant magnetic scattering (XRMS). In addition to the reduction of the magnetization, we report an ultrafast change of the magnetic chirality occurring in the first few picoseconds after optical pumping. Then the XRMS signal, related to the homochiral Néel domain wall periodicity is recovered faster than the domain magnetization and subsequently accompanied by a 6 GHz oscillation lasting up to nanosecond time scales. We attribute the short timescale XRMS dichroism reduction in the diffracted intensity to the spin current induced coherent and incoherent torques within the continuously varying spin texture of the domain walls. We argue that the specific demagnetization in the domain walls induces a flow of hot spins from the interior of the domains that distort their homochiral Néel shape into transient mixed Bloch-Néel-Bloch textures. Time-resolved circular dichroism in XRMS can be a unique tool for studying the time evolution of the type and the chirality of the magnetic phase of any ferroic (magnetic, electric, multiferroic) material. Similar investigations could be profitably extended to other systems showing a non-collinear electric/magnetic ordering such as skyrmion lattices or conical/helical phases stabilized by the DM interaction, as well as more complex systems such as the recently observed antiskyrmion lattices, in metallic or insulating materials.

Main text:

Chirality is a central concept in science and, in condensed matter, a large variety of physical phenomena hinge on the emergence of complex chiral windings of order parameters. The observation of these complex chiral windings and subsequent control are an important issue. In particular, in magnetism chirality has attracted a huge renewed interest since the first evidence of a skyrmion lattice

phase obtained by neutron scattering [1]. It was realized that these magnetic textures are stabilized by the Dzyaloshinskii-Moriya (DM) interaction, which is the antisymmetric analog of the Heisenberg interaction [2,3]. The DM interaction requires spin-orbit coupling (SOC) and broken inversion symmetry, found either in specific crystalline structures such as B20 materials [4] and at thin film [5,6] or multilayers [7-9] opening the possibilities to stabilize and control chiral magnetic textures. We have recently shown that dichroism in x-ray resonant magnetic scattering (XRMS) is a powerful tool to determine their characteristics, *i.e.*, their type (Néel or Bloch) and sense of rotation (chirality) in ferromagnetic multilayers [10]. Moreover, performing XRMS on several multilayers made of stacks with different numbers of trilayers, comprising a magnetic layer sandwiched in between two different non-magnetic materials, we demonstrated that hybrid chiral spin textures in the direction perpendicular to the film plane can be realized. This hybrid chirality results from the competition between the different magnetic interactions and can be stabilized in these multilayers even with a limited number of repeats [11]. Such hybrid chiral configurations have been confirmed by Lorentz microscopy [12,13]. The static (size, shape, stability) as well as dynamic properties (spin torque induced motion) properties of these chiral domain walls or skyrmions are currently topics of intense research [14-18].

However, the ultra-fast behavior of these chiral textures as well as the timescale for establishing the DM interaction is almost unexplored. To address directly this open question directly we carried out time-resolved XRMS experiments at the DiProI beam line [19] of the FERMI free electron laser [20] located in Trieste (Italy). This pump-probe experiment is schematized in Fig. 1, where a fs x-ray pulse is used to probe the ultrafast time evolution of the amplitude of the circular dichroism in XRMS after a laser induced demagnetization. The studied system is a magnetic

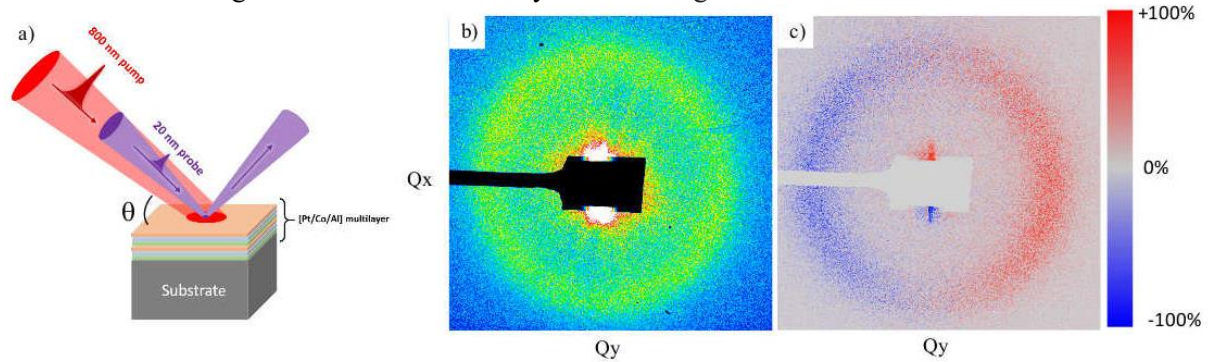


Figure 1: XRMS measurements at the Fermi beamline. (a) Principle experimental configuration with both x-ray and IR incident beams impinging on the sample. (b) XRMS pattern, (CL+CR) corrected for the geometrical projection angle. (c) Dichroic pattern obtained (CL-CR), displaying the typical signature of a clockwise (CW) Néel domain wall.

multilayer $\text{SiO}_2|\text{Ta}(5)|\text{Pt}(8)|[\text{Co}(1.5)|\text{Al}(1.4)|\text{Pt}(3)]_x4|\text{Co}(1.5)|\text{Al}(1.5)$ (thicknesses in nm) (see Ref. [21] and Supplementary Sec. S1 for details) with perpendicular anisotropy and a large interfacial DM interaction. As displayed in the scattering diagram (Fig. 1(b)), such a multilayer has a characteristic randomly disordered magnetic stripe pattern with a mean period of about 330 ± 30 nm, corresponding to an average domain size of 165 ± 15 nm. Following the approach used in Ref. [10], a preliminary static XRMS characterization (see S1) at the Co L edge at remanence after a field demagnetization has been performed on the SEXTANTS beamline at synchrotron SOLEIL, France [22], confirming that magnetic worm domains with homochiral clockwise (CW) Néel domain walls are stabilized. Moreover, from micromagnetic calculations with MuMax3 [23] (details about the simulations are included in Supplementary Sec. S1), we can extract the width of the domain wall. The detailed study of the micromagnetic effective properties corresponding to the studied sample is used to feed the empirical XRMS simulations with accurate parameters, notably the actual width (as defined below) of the domain wall (DW) that is found to be ~ 22 nm (see S1 for details).

The pump-probe measurements were conducted in reflectivity geometry using circularly left (CL) and right (CR) incident x-ray beam polarizations at the Co M edges (photon energy ~ 60 eV). While this technique can be sensitive to electronic and spin dynamics, we note that in this study we are only interested in the spin dynamics. We performed the experiment at the main absorption energy to ensure insensitivity to any shift of the edge at ultrafast timescales [24]. The diffracted x-rays are collected using

a Peltier-cooled square CCD detector located 12 cm away from the sample. Typical XRMS patterns of the domain structure are displayed in Fig. 1(b,c). Note that the images have been geometrically corrected to account for the projection related to the photon incidence angle $\theta = 45^\circ$. In Fig. 1(b), we display the intensity sum of CL and CR polarized beam images representing the magnetic contrast of the periodic structure, i.e. the total magnetic scattering intensity, which comes mainly coming from the magnetic domains. In Fig. 1(c), the ratio $(CL-CR)/(CL+CR)$ is presented [10, 25], it is also related to the ratio of in-plane to out-of-plane moments. The change of sign on either sides of the specular reflection indicates the presence of chirality and the sense of rotation inside the DWs [10]. The dichroism recorded at the Co M edge mimics the one recorded at the L edge. It should also be mentioned that at the Co M edge, the penetration depth is of the order of 10 nm in this geometry at 45° incidence, thus mostly the upper Co layer is probed in these measurements. These XRMS diffraction diagrams have been recorded in pump-probe scheme by varying the delay between the IR pump and the x-ray probe up to 900 ps with an inhomogeneous temporal step size adapted to the main time scale of the sample response. At FERMI, the pulse duration is about 60 fs for the x-rays and 100 fs for the IR (780 nm wavelength) respectively, giving a combined time resolution of about 120 fs. The two beams had a 2° angular offset and a filter opaque to IR was mounted in front of the CCD to block any IR light and allow only the x-rays to impinge on the CCD. We chose the IR pump fluence and the probing energy very carefully. Importantly, the infrared IR laser fluence is much lower than the one that caused a change of electron occupation induced by the IR pulse using x-ray absorption spectroscopy (XAS) [26]. We performed a series of measurements using several IR fluences with a X-ray fluence that has to be properly adapted in order to not modify the sample and measure meaningful experimental data. Importantly, we found that when the FEL fluence is too intense, it can reduce the magnetic chirality by inducing a modification of the multilayer properties during the two-hours long acquisition (see Supplementary Sec. S2). All X-ray results presented in the paper have been recorded using conditions that did not modify the sample, i.e., an IR fluence of 4.8 mJ/cm^2 and a FEL fluence of 0.5 mJ/cm^2 . The latter condition was determined by reducing by 50% the FEL intensity with respect to when a detectable degradation of the sample response was observed. For each delay and each X-ray polarization, 500 scattering patterns have been recorded, normalized to the incident flux and then averaged. In order to extract both the total magnetic scattering intensity (sum) and the magnetic dichroism (difference), we also subtracted a background signal recorded before and after each run. After data acquisition, a radial integral of the diffraction pattern (See Fig. 1) is performed over the region of interest. This allows us to fit the $CL+CR$ and $CL-CR$ signals by a Gaussian to extract the integral, the full width at half maximum (FWHM) and the position of the magnetic intensity for each time delay. Details of the analysis procedure are presented in Sec. S3.

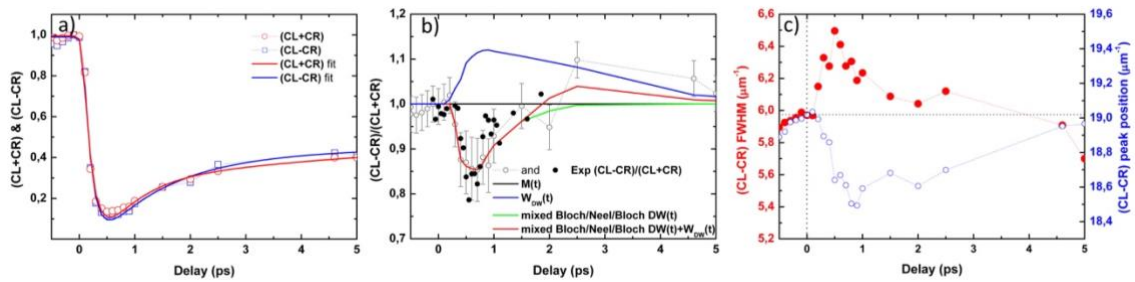


Figure 2: Short timescale temporal experimental evolution of (a) the intensity of integrated diffraction ring ($CL+CR$) and dichroism ($CL-CR$) normalized to one before the pulse. (b) Experimental asymmetry ratio $(CL-CR)/(CL+CR)$ in open grey and filled dots with simulations for different models (see text and Supplementary Sec. 5 for details). (c) FWHM (red circles) and mean position (open blue dots) in reciprocal space of the magnetic dichroic peak as a function of time.

One of the first observations from the raw data (Fig. 2(a)) is that both $CL-CR$ and $CL+CR$ signals behave very similarly: $CL-CR$ (blue open squares) related to the magnetic chirality and $CL+CR$ (red open circles) reflecting the total magnetization, are strongly diminished within the same timescale of 150 ± 30 fs. We first focus on the few picoseconds after optical pumping. The magnetic intensity has been fitted (blue solid line in Figure 2 a) using the phenomenological function of three different exponential with time constants related to the ultrafast demagnetization, fast recovery and long-time recovery from the quenched state [27-29]. We then proceed with the same analysis for the dichroism [red solid line in Figure 2(a)]. Our main experimental results in this ultrashort time window can be more

explicitly highlighted by plotting the asymmetry ratio of the dichroism divided by the magnetic intensity, *i.e.* $(CL-CR)/(CL + CR)$ as shown by open gray dots in Fig. 2(b). We repeated the experiment a second time, shown in black dots giving a good estimate of our experimental error bar. A clear deviation from one appears after 0.3 ps and this ratio remains below 1.0 until around 1.5 ps. This behavior is not consistent with a picture of completely homogeneous behavior where the magnetic moments decrease/increase by the same amount simultaneously in both domains and DWs, which would result in an asymmetry ratio of 1. In consequence, an asymmetry ratio lower than 1 unambiguously indicates a larger reduction of the magnetic chirality, *i.e.* the magnetization in the DWs, as opposed to the adjacent domains.

In order to better understand this observation, we believe that it is important to first recall the salient features of ultra-fast demagnetization. Several mechanisms have been proposed to explain the loss of magnetization induced by a strong laser pulse. They generally relied on the conservation of angular momentum during the demagnetization process. Among them, we can cite local mechanisms using the coupling between the photon field and the spin bath [30] or spin-flip processes during electron-electron scattering [31], as well as the interactions with phonons [32] and magnons [33]. Another mechanism related to spin dependent transport of hot electrons has been recently shown to play an important role in angular momentum dissipation during ultrafast processes. This mechanism has been first experimentally demonstrated in spin valves where demagnetization is faster for the antiparallel magnetic layers [34] and some models based on polarized electron transport in the superdiffusive regime have been subsequently developed [35]. The optically excited, initially ballistic, hot electrons with spin-dependent lifetimes and velocities generate out-of-equilibrium spin currents either within a ferromagnetic layer, or outside, *e.g.*, in an adjacent heavy metal layer where spin-charge conversion can also result in the generation of intense THz pulses at the ps timescales [36]. The existence of laser induced hot electron spin transport was clearly evidenced [37] and it is now widely accepted that the induced loss of angular momentum greatly participates in ultrafast magnetization dynamics [38]. This idea has also been tested in single layers with a heterogeneous magnetization state, *i.e.*, containing a large density of magnetic domains and domain walls, albeit with different conclusions [38, 39]. X-ray diffraction experiments are here more powerful for probing the behavior of DWs [40-42]. In the work of Pfau *et al.* [40], it was inferred from the variations of the first-order Bragg peak of the magnetic configuration, that the DW size changes in the first few ps. More recently, Zusin and coworkers have highlighted that a more reliable way to extract DW information is to study the positions and widths of higher order diffraction peaks [41]. Unfortunately, in our reflection geometry, the large contribution of a diffuse background from the specular intensity makes the first approach unreliable. Moreover, the second method is not applicable due to the long x-ray wavelength. However, the position of the magnetic dichroic peaks is also related to the DW width and its FWHM provides information on the correlation length. These two quantities are displayed in Fig. 2(c) for our sample. A clear decrease of the mean peak position around 1 ps is observed, equivalent to an apparent increase of the DW size of the pumped system. We conclude that this is a signature of an ultrafast *spatial* response of the domain wall. Again, this DW expansion starts only after 0.3 ps, *i.e.*, after the ultrafast demagnetization regime, and expands up to 0.9 ps when the fully quenched magnetization starts to recover. Then the DW mean size remains expanded until it transiently recovers its nominal size around 5 ps.

The understanding of the DW width expansion requires considering the intense flow of spin currents in the ps regime. It is known [36] that these currents can efficiently transfer angular momentum to the Pt where the large spin-orbit interaction quenches it. This results in an enhanced demagnetization as well as faster magnetization recovery. Our interpretation is that any source of angular momentum dissipation will have a similar effect, and in particular, the one induced by non-collinearity within the sample, and notably inside the domain walls. Interestingly, the behavior of a spin current crossing a domain wall has been studied in the past in relation to the observed extra resistance associated to DWs as well as the induced spin transfer torques which eventually results in their displacement. In particular, ballistic models seem particularly well adapted to the ultrafast demagnetization scenario where superdiffusive spin currents play a central role. The behavior of ballistic spin carriers was introduced in the first measurement of domain wall resistance [44] and can be described within two equivalent points of view, *i.e.* a classical spinned particle perceiving a time varying exchange field while crossing the wall

[44, 45], or a quantum transport of spin up and down carriers having different momenta [46, 47]. As both views are equivalent (see *e.g.* Ref. [47]), we adopt here the former description detailed in Ref. [45], which is easier to visualize. A few basic facts have to be underlined in order to grasp the spin evolution of the ballistic electrons. First, these are band particles which are coupled by exchange to the localized spins (this is the so-called *s-d* Hamiltonian). Their velocity perpendicular to the wall is related to their momentum in *k*-space. With the appropriate parameter renormalization, the problem is equivalent to the “fast adiabatic passage” known, for example, in NMR theory. The spin evolution is given by the Landau-Lifshitz equation:

$$\frac{d\vec{\mu}}{dt} = \frac{J_{ex}S}{\hbar} \vec{m} \times \vec{\mu}$$

where $\vec{\mu}$ is the electron spin, $J_{ex}S$ the exchange energy with the localized moment (*S*), and \vec{m} the direction of the time varying exchange field seen by the ballistic electrons. Spins are indeed rotating in a Néel fashion within the walls and the problem is generally treated in this rotating frame [45]. In essence, the spins want to precess and thus acquire a component out of the plane of rotation, inducing a torque globally parallel to the chiral vector: $S_i \times S_j$. The electron spin mistracking angle ω is proportional to the velocity *v* divided by the exchange times DW width Ref. [44]: $\langle \omega \rangle = \frac{\pi \hbar v}{S J_{ex} DW}$ Typically, for electrons at the Fermi level, this angle is about 7° for a DW width of 15 nm [45]. However, it can be anticipated to be quite different for the hot electrons produced in the demagnetization process and the relevant parameter values are hard to quantify. If velocities near 10⁶ m/s are considered, *i.e.*, not far from that at the Fermi level [36], exchange energies in bands over 1 eV above the Fermi level can be dramatically lower around 0.1 eV or even below 1 eV. However, incoherent spin currents flowing in all directions in the DW shall reduce the possible net angular deviation of hot spins (making them to follow the space derivative of the wall profile) and hence decrease the resulting net torque on the DW. Therefore, the obtained global effect is mainly longitudinal as disorder in precession induced by non-collinearity results in an average loss of angular momentum. In turn, this should speed up the spin relaxation processes so that after some 100 fs, a net spin current should be established from the domains to the interior of the DWs. The resulting effect generates a stronger torque from the coherent evolution of the hot electron spins on the localized moments in the DW. This induces a net magnetization tilting out of the Néel plane as illustrated in Figure 3(a), resulting in a new transient DW shape depicted in Figure 3(b). Such a mixed Bloch/Néel/Bloch contribution will in turn result into a transient reduction of the measured chirality as it adds two (opposite) Bloch components on both sides of the walls to the originally purely Néel character. In order to estimate the amplitude of this distortion, it is useful to realize that unlike small current-induced electron flows at the Fermi level, spin fluxes during demagnetization are enormous as, at the fluence of the experiment, typically 0.5 electrons per Co atom per pulse are excited to higher bands. The torque then acts oppositely between the local magnetization and the hot spin population, with a typical timescale given by the exchange energy. For spin temperatures sufficiently different between domains and DWs, a quantitative estimate using the abovementioned parameters gives a tilting angle of great than 10°. Moreover, it has to be noticed that the onset of this Bloch component in the DW leaks out into the domains, thus slightly increasing the effective DW width.

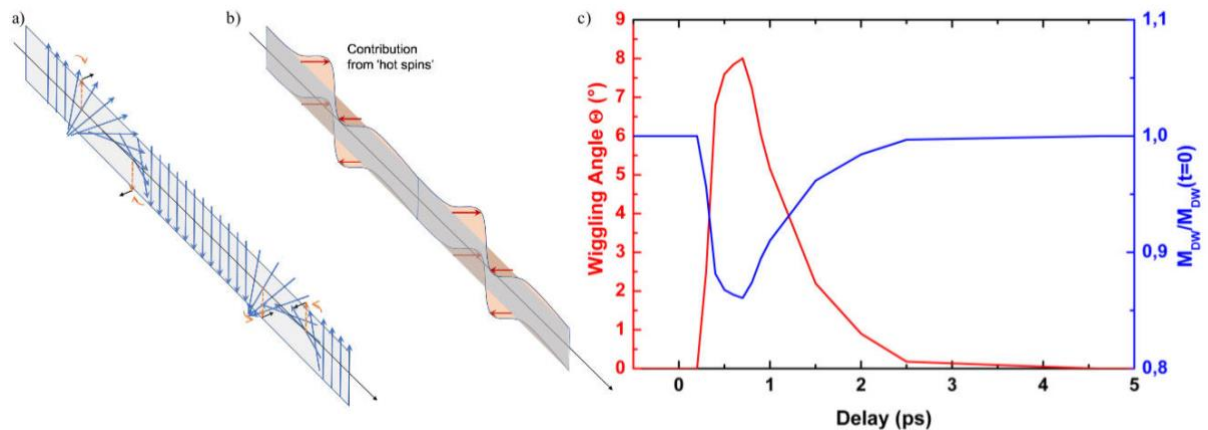


Figure 3: Magnetization texture modification by hot electrons. (a) Schematic representation of the torque (black arrows) imposed by the 'hot spins' flowing from the domains to the domain walls resulting in transient mixed Bloch/Néel/Bloch contributions. (b) Transient DW shape. (c) wiggling angles (red) and DW magnetization (blue) used in the simulations of the asymmetry ratio shown in Fig. 2(b)

Using a 1D magnetization profile (described in Supplementary Secs. S4 and S5) and taking into account the experimental change of magnetization (extracted directly from the square root of the (CL+CR) intensity), the time evolution of the asymmetry ratio can be simulated. The sole homogeneous change of magnetization amplitude does not affect the asymmetry ratio. In a further step to understand the (CL-CR)/(CL+CR) time dependence, we also need to account for the measured expansion of the domain wall directly derived from the variation of the magnetic peak position shown in Fig. 2(c). The simulation shown in blue in Fig. 3(c) results in an asymmetry ratio increasing above 1, as the proportion of chiral volume increases in the sample. We then estimate from simulation the asymmetry ratio for the proposed DW broadening mechanisms, including both incoherent and coherent effects. We consider a magnetization in the domains extracted from the CL+CR data, along with a further 13% reduction of the magnetization inside the DWs to account for incoherent effects, as well as a transient Bloch/Néel/Bloch wall as shown in Fig. 3(a) for coherent ones. One should note that these Bloch contributions are expected to give a dichroic signal at another position in reciprocal space, however not accessible in the present experimental geometry. A rotation angle of $\sim 8^\circ$ gives excellent agreement with the data (green curve in Fig. 2(b) and even accounting for DW expansion [red curve in Fig. 2(b)], the agreement can be obtained for a $\sim 11^\circ$ tilt angle. Interestingly, the DW distortion is expected to be established very fast because the process stemming from excited electrons is exchange driven (below 100 fs) but should last for much longer time given by the micromagnetic processes (nanosecond scale). On the other hand, the incoherent part relaxes at the ps timescale of remagnetization processes as measured in the experiment. Interestingly, in the DWs, remagnetization should be faster and the asymmetry ratio can exceed 1, as measured. The behavior of both quantities can therefore be qualitatively understood using the hot spin currents driven vision described previously. Indeed, the diffraction peak is affected by the dispersion of DW spacing and width. In the lines of the torques acting on DWs, it is known that any defect or kink in the structure will sensitively amplify the precession angles, and hence the local torques [45]. This should enhance coherent and incoherent processes both diminishing the contribution of kinks or steep geometrical asperities. The expected effects are a loss in the high q side of the distribution and an increase in the variability of the Bloch (coherent) or spin temperature (incoherent) variations within the DWs. The former would shift the peak position to lower angles and the latter increase the distribution width, exactly as observed in Fig. 2(c).

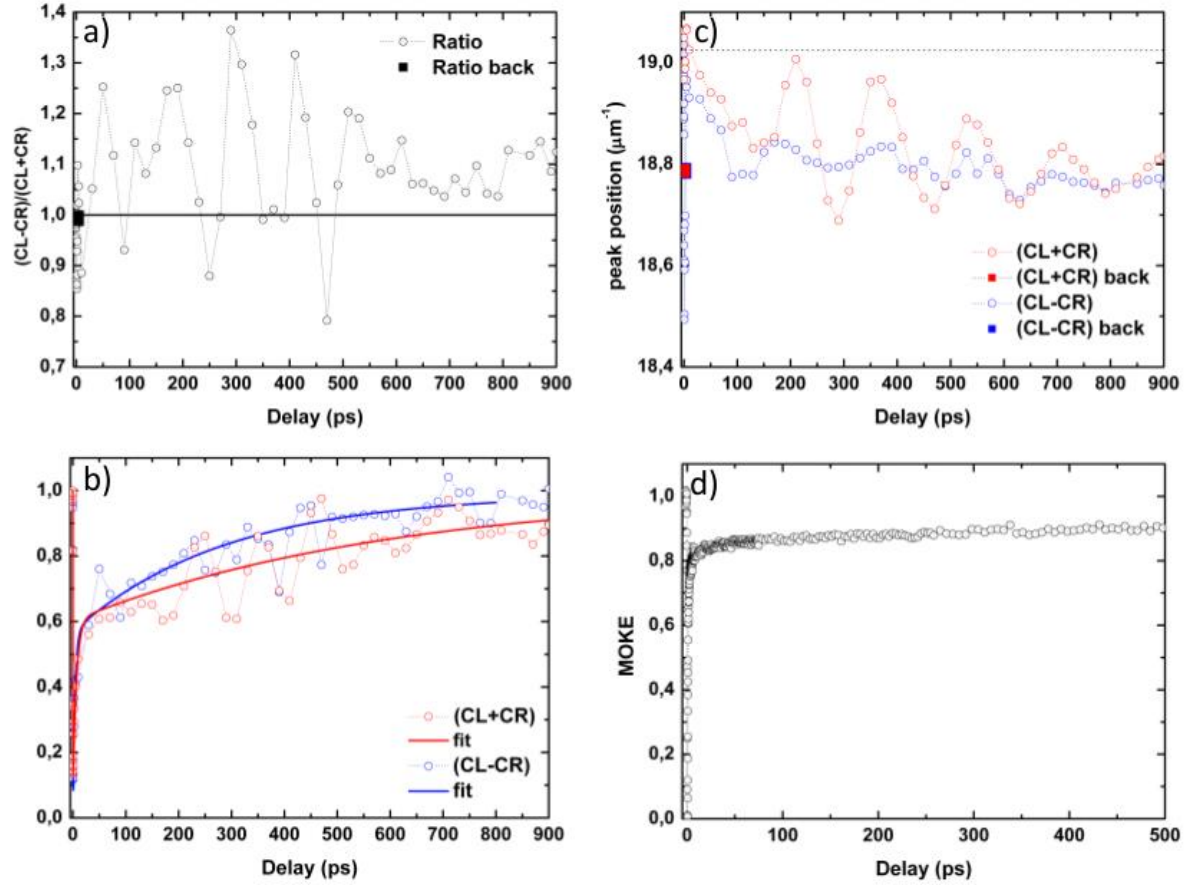


Figure 4: (delay scan a) Evolution of the magnetic asymmetry ratio $(CL-CR)/(CL+CR)$. The black square represents the measurement at equilibrium (delay = -1 ps) recorded few minutes after the “delay scans”. (delay scan. b) Evolution of $(CL+CR)$ and $(CL-CR)$ and the fit using the three-exponentials model as explain in Supplementary Sec. S4. (c) $(CL+CR)$ and $(CL-CR)$ peak position. The red/blue squares represent the measurement at equilibrium (delay = -1 ps) recorded a few minutes after the “delay scans”. (delay scan d) Time resolved MOKE recorded on the same sample (see Sec. S3).

We also record the magnetic ring intensity and the dichroism up to 900 ps in order to investigate the magnetic dynamics of the chirality over a longer timescale. First, we find that the magnetic asymmetry ratio exceeds 1 around a few 10 ps and its amplitude oscillates as the system relaxes back towards equilibrium. The solid black square dot corresponds to a data point recorded a few minutes after the delay scan for a delay of -1 ps. In the long delay time regime, an oscillation is observed with a frequency of about 6 GHz, especially in the $(CL+CR)$ signal shown in Fig. 4(b). The same figure also shows that the dichroism recovers faster, indicating that DWs relax and magnetize faster than the domains after a few tens of ps. The time constant estimated from fitting (details in Sec. S4) is 290 ± 20 ps for the dichroism and 600 ± 30 ps for the total intensity, as illustrated in Fig. 4(b). Fig. 4(c) shows the time evolution of magnetization $(CL+CR)$ and chiral $(CL-CR)$ signal peak positions. Unlike the signal intensities of (Fig. 4(b)), where long time scale oscillations are only visible in the magnetic contribution, the positions of maximum scattering intensity both oscillate with a 6 GHz period. Interestingly, the time-resolved MOKE measurements of Fig. 4(d) (and Sec. S6) taken at saturation show a smooth behavior with no oscillation. We take this as evidence for the role of DWs in launching excitations in the whole system. However, phonons [48] or other magneto-acoustic modes do not fall in this range of frequencies. Broadband vector network analyzer ferromagnetic resonance (VNA-FMR) (Sec. S7), and theoretical modeling based on theory developed in Ref. [49] (Sec. S8) exclude the presence of ‘classical’ modes below 15 GHz. From simulations (Sec. S8), we find that a lower energy mode at zero field (sample in demagnetized state) using the magnetic parameters determined experimentally is around 15.6 GHz in excellent agreement with VNA-FMR (Sec. S7). However, it is important to note that during remagnetization the magnetic anisotropy is expected to vary significantly, thus changing the intrinsic parameters of the system from the equilibrium room-temperature values. This makes the discrepancies with simulations and FMR less meaningful for these intermediate timescales.

In conclusion, we report here on an experimental investigation of the picosecond time domain evolution of complex chiral spin textures after laser induced demagnetization. For that, we employ circular dichroism in XRMS to obtain information in the time domain on both the magnetic domain configuration and the magnetic chirality. Beyond the evolution of the magnetic period in magnetic multilayers with large perpendicular anisotropy, we investigate how the chirality of the non-collinear spin texture, and their long-range ordering, evolves in the few ps after a strong optical pulse. We observe that the magnetic asymmetry ratio reflecting the domain wall properties demagnetizes faster than the domain magnetization in the first 2 ps after the laser pulse. To explain this unexpected change of effective chirality on this timescale, we propose that hot spins flowing from the interior of the domains inside the domain walls induce an ultra-fast distortion of the DW magnetization. This leads to a transient mixed Bloch-Néel-Bloch domain wall accompanied by reduction of the magnetization inside the DW. Our simulations, considering the measured timescales and the DW expansion, can reproduce the experimental asymmetry ratio when including a magnetization reduction of 13% with an 8° distortion of the DW. After a few ps, the DWs return to a homochiral Néel configuration preserving the original sense of rotation (*i.e.*, chirality) and relaxes with ~6 GHz oscillations in size lasting for the few 100 ps of the magnetization recovery. At longer timescale, the whole system relaxes towards its equilibrium and the original homochiral Néel type system is restored. We would like to stress that our approach using dichroism in XRMS is applicable to any other magnetic chiral texture and should provide a better understanding of the evolution of the chirality of spin texture on the ultrafast timescale.

Acknowledgment: We would like to acknowledge Ivaylo Nikolov, Michele Manfreda Luca Giannessi and Giuseppe Penco for their inestimable help to set up the FEL and the laser for our experiment. NJ would like to thank S. Flewett for discussion on XRMS simulations. Financial supports from FLAG-ERA SographMEM (ANR-15-GRFL-0005), Financial the Agence Nationale de la Recherche, France, under grant agreement no. ANR-17-CE24-0025 (TOPSKY) and 18-CE24-0018-01(SANTA), the Horizon2020 Framework Program of the European Commission under FET-Proactive Grant agreement no. 824123 (SKYTOP). E. J. is grateful for financial support received from the CNRS-MOMENTUM. O. S. L., A. V. S., and V. V. K. acknowledge funding from the Engineering and Physical Sciences Research Council of the United Kingdom (Grant No. EP/T016574/1).

References:

- [1] S. Mühlbauer et al., Science 323, 915 (2009).
- [2] I. Dzyaloshinskiy, J. Phys. Chem. Solids 4, 241 (1958).
- [3] T. Moriya, Phys. Rev. 120, 91 (1960).
- [4] X. Z. Yu et al., Nature 465, 901 (2010).
- [5] M. Bode et al, Nature, 447, 190 (2007)
- [6] S. Heinze et al Nat. Phys., 7, 713 (2011)
- [7] A. Fert, Mater. Sci. Forum 59, 439 (1990).
- [8] A. Thiaville et al., EPL 100, 57002 (2012).
- [9] A. L. Balk et al., Phys. Rev. Lett. 119, 077205 (2017).
- [10] J.-Y. Chauleau et al., Phys. Rev. Lett 120, 037202 (2018)
- [11] W. Legrand et al., Sci. Adv. 4, eaat0415 (2018)
- [12] K. Fallon et al., Phys. Rev. B 100, 214431 (2019).
- [13] M. J. Benitez et al., Nat. Commun. 6, 8957 (2015).
- [14] A. Thiaville et al., Euro. Phys. Lett. 100, 57002 (2012)
- [15] K.S. Ruy et al., Nature Nanotech 8, 527 (2013)
- [16] N. Nagoasa and Y. Tokura, Nat. Nanotech. 8, 899 (2013)
- [17] A. Fert, N. Reyren, V. Cros, Nat. Rev. Mat. 2, 17031 (2017)
- [18] S. Yang, K., Ryu, K. & S. Parkin, S., Nature Nanotech 10, 221–226 (2015).
- [19] F. Capotondi et al., Rev. Sci. Instrum. 84, 051301 (2013).
- [20] E. Allaria et al., Nature Photonics 6 (10), 699 (2012)
- [21] C. Moreau-Luchaire et al., Nat. Nanotech. 11, 444 (2016).

- [22] M. Sacchi et al., J. Phys. Conf. Ser. 425, 072018(2013).
- [23] A. Vansteenkiste et al. AIP Adv. 4, 107133 (2014).
- [24] K. Yao et al., <https://arxiv.org/abs/2005.02872>
- [25] H.A. Dürr et al, Science 284, 5423, 2166 (1999).
- [26] B. Mathieu et al., Nat. Comm. 9, 3276 (2018).
- [27] E. Beaurepaire et al., Phys. Rev. Lett. 76, 4250 (1996).
- [28] F. Dalla-Longa et al., Phys. Rev. B 81, 094435 (2010)
- [29] C. Boeglin et al., Nature 465, 458-461 (2010).
- [30] J.Y. Bigot et al., Nat. Phys. 5, 515 (2009)
- [31] M. Kraub et al., Phys. Rev. B 80, 180407 (2009)
- [32] B. Koopmans, et al. Nat. Mater. 9, 259 (2010) and K. Carva, et al., Phys. Rev. B 87, 184425 (2013)
- [33] F. Carpena, et al., Phys. Rev. B 78, 174422 (2008)
- [34] G. Malinowski, et al., Nat. Phys. 4, 855 (2008)
- [35] M. Battiato et al., Phys. Rev. Lett. 105, 027203 (2010)
- [36] T. Kampfrath et al., Nature Nano. 8, 256 (2013).
- [37] A. Melnikov et al. Phys. Rev. Lett. 107, 076601 (2011)
- [38] B. Vodungbo et al., Nat. Commun 3, 999 (2012)
- [39] B. Pfau et al., Nat. Comm. 3, 1100 (2012).
- [40] D. Zusin et al., <https://arxiv.org/abs/2001.11719>
- [41] N. Kerber et al., <https://arxiv.org/abs/2002.03971>
- [42] M. Hennes et al., arXiv <https://arxiv.org/abs/2006.11246>
- [43] N. Moisan et al., Scientific Reports, 4658 (2014)
- [44] M. Viret et al., Phys. Rev. B 53, 8464 (1996).
- [45] A. Vanhaverbeke and M. Viret, Phys. Rev. B 75, 024411 (2007).
- [46] P.M. Levy and S. Zhang, Phys. Rev. Lett. 79, 5110 (1997).
- [47] X. Waintal and M. Viret, Europhys. Lett. 65, 427 (2004).
- [48] E. Jal et al., Phys. Rev. B 95, 184422 (2017).
- [49] N. J. Whitehead et al., Phys. Rev. B 96, 064415 (2017).

Supplementary

Ultrafast time-evolution of magnetic chirality probed by circular dichroism in x-ray resonant magnetic scattering in homochiral skyrmionics systems

Cyril Leveillé¹, Erick Burgos-Parra^{1,2}, Yanis Sassi², Fernando Ajejas², Valentin Chardonnet³, Emanuele Pedersoli⁴, Flavio Capotondi⁴, Giovanni De Nino^{4,5}, Francesco Maccherozzi⁶, Saranjeet Dhesi⁶, David M. Burn⁶, Gerrit van der Laan⁶, Oliver S. Latcham⁷, Andrey V. Shytov⁷, Volodymyr V. Kruglyak⁷, Emmanuelle Jal³, Vincent Cros², Jean-Yves Chauleau⁸, Michel Virets, Nicolas Reyren², and Nicolas Jaouen¹

¹Synchrotron SOLEIL, Saint-Aubin, Boîte Postale 48, 91192 Gif-sur-Yvette Cedex, France

²Unité Mixte de Physique, CNRS, Thales, Univ. Paris-Saclay, 91767 Palaiseau, France

³Sorbonne Université, CNRS, LCPMR, 75005 Paris, France

⁴Elettra-Sincrotrone Trieste, 34149 Basovizza, Trieste, Italy

⁵University of Nova Gorica, 5000 Nova Gorica, Slovenia

⁶Diamond Light Source, Harwell Science and Innovation Campus, Didcot, Oxfordshire, OX11 0DE, UK

⁷University of Exeter, Stocker road, Exeter, EX4 4QL, United Kingdom.

⁸SPEC, CEA, CNRS, Université Paris-Saclay, 91191 Gif-sur-Yvette, France

S1. Sample growth and characterization

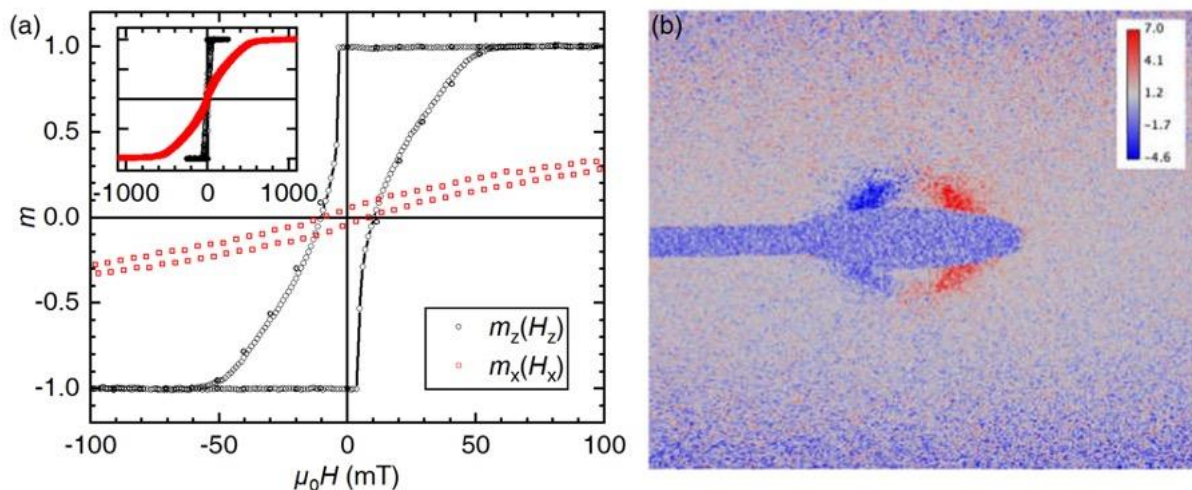


Figure S1: Characterization of the sample magnetic properties. (a) In plane (AGFM) and out-of-plane (Kerr) normalized magnetization loop. SQUID measurement on twin sample indicate that $M_s = 1069$ kA/m. (b) Circular dichroism in XCMS measured at Co L_3 edge (778.2eV) in percent, corresponding to CW Néel DW.

The metallic multilayers are grown by magnetron sputtering at room temperature on thermally oxidized Si substrates. The sample at the center of our study is $\text{SiO}_2|\text{Ta}(5)|\text{Pt}(8)|[\text{Co}(1.5)|\text{Al}(1.4)|\text{Pt}(3)]_x4|\text{Co}(1.5)|\text{Al}(1.5)$; numbers in parentheses correspond to

thickness in nm. The top Al layer is oxidized using 50 mbar of O₂ before being exposed to air. In order to maximize the photon transmission at 60 eV, but still avoiding oxidation of the Co layer, an optimal thickness of 1.5 nm Al as capping layer has been used. Reducing as much as possible the thickness of the capping is crucial for the quality of the XRMS data reported in this article. Using SQUID and alternating gradient force magnetometer (AGFM), a saturation magnetization $M_s \approx 1$ MA/m and a large out-of-plane anisotropy $K_{\text{eff}} \approx 0.2$ MJ/m³ is measured. Following the approach used in Ref. [7], we checked that the sample top layer displays magnetic worm domain with a homochiral clockwise (CW) Néel Domain wall (DW) determined with XRMS measure at Co L_3 edge at the SEXTANTS beamline [16] of the SOLEIL synchrotron as displayed in Fig. S1(b).

To model the domain wall textures, we use the MuMax3 code [18, S1, S2]. We used cell volumes of about $0.64 \times 0.94 \times 1.48$ nm³ along x, y and z directions. The system size was $(270 \pm 20) \times 30 \times 25.1$ nm³ with periodic boundary conditions along x and y (SetPBC(16, 64, 0)). Note that we considered a period of 270 nm for stripe domains, a value different from the one found in the labyrinthine state (330 nm). We did not consider any electronic exchange between the magnetic layers. The magnetization is initialized with two domains, magnetization pointing along +z for smaller x, and along -z for larger x; the central domain wall is set along the [1 1 1] direction, the domain wall on the external side has zero width. The magnetization is minimized from this state. The set of micromagnetic parameters should be self-consistent and match several observations:

1. VNA-FMR measurements indicate an effective anisotropy of about 235 kJ/m³ (Sec. S8).
2. The period of the stripes (after in-plane demagnetization) is 270 nm as measured by MFM in the stripe configuration.
3. XRMS data indicate a CW DW chirality for the top layer, while the mean chirality is CCW.

Using the SQUID experimental measurement of $M_s = 1069$ kA/m, we calculate the effective uniaxial anisotropy to be $K_u = 953$ kJ/m³ to match observation (1). The exchange and the effective DMI in the system are the parameters that are the more difficult to measure. Therefore, we explored the range of possible parameters that would match observation (2), i.e., the domain period p_0 . This is realized by calculation of the energy density ε of the system for fixed parameters, but using different periods p , slightly longer or larger than the observed one. We can then calculate the numerical derivative of the energy density at the observed period p_0 for a set of effective parameters for the symmetric exchange A and the DMI asymmetric exchange D (Fig. S2(a)). Finally, looking at the chirality of the top layer of the simulated multilayer DW, we can check values satisfying observation (3) (Fig. S2(b)). We end up with a range of possible A and D parameters: $9 < A < 12$ pJ/m and $D < 1.2$ mJ/m². From other studies using Brillouin light scattering and DW propagation [Sec. S3], we expect $D \approx 1$ mJ/m² for this particular stack.

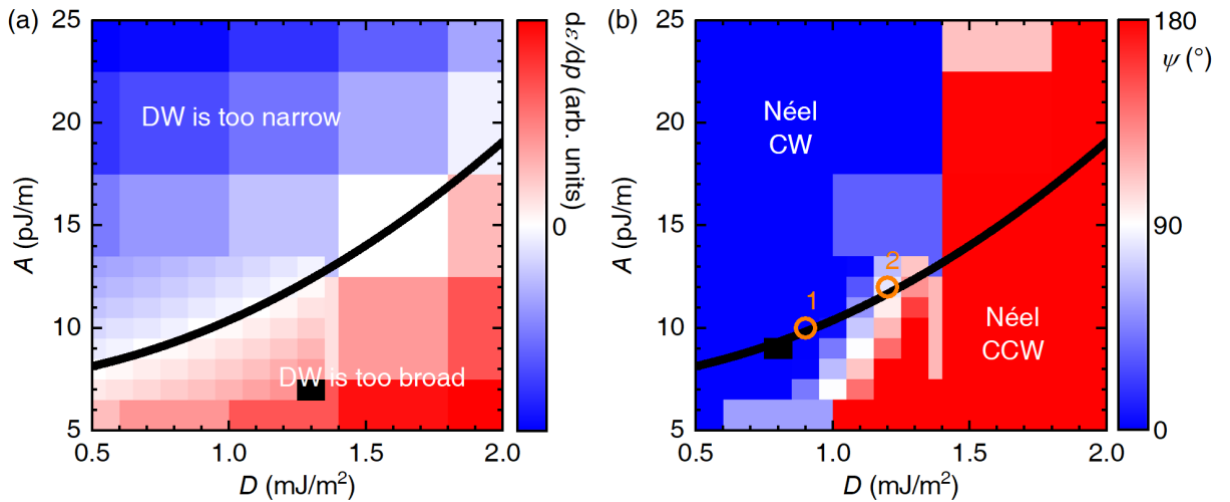


Figure S2: Determination of the symmetric and antisymmetric exchange energies. (a) Map of the derivative of the energy density ε by the domain period p as a function of the effective DMI D and effective exchange energy A . The zero-derivative indicated by the thick black line corresponds to the set of possible parameters minimizing the energy density for the observed period $p_0 = 270$ nm. (b) Corresponding map of the domain wall magnetization angle ψ of the top Co layer. The curve of the

possible parameters is reported from panel a. The Bloch component is determined by the initial condition of the simulation and is always around $\psi = 90^\circ$. Black squares indicate discarded values. Enumerated orange circles correspond to selected parameter sets for Fig. S3.

We explored in details the DW profile of two cases (orange circles in Fig. S2) close to these values and use them to determine the width parameter of the empirical model of the XRMS analysis. In Fig. S3 are displayed the three components of the magnetization profiles of these two “extreme” parameter sets; set 1: $A = 10$ pJ/m, $D = 0.9$ mJ/m²; set 2: $A = 12$ pJ/m, $D = 1.2$ mJ/m². The width of the z-component is practically unchanged and takes the value 20.9 nm and 18.2 nm for set 1 and 2, respectively. The empirical XRMS model profile shows a slight inconsistency concerning the width of the other components, taking the values 23.1 nm (set 1) and 55 nm (set 2) for the x component and 18.1 nm for the y component. In Set 1, the magnetization of the wall in the top layer is “pure Néel CW”, while it is mostly Bloch in Set 2 with a minute CW Néel component. The Bloch part is *a priori* achiral, meaning that it does not appear in the CD-XRMS images.

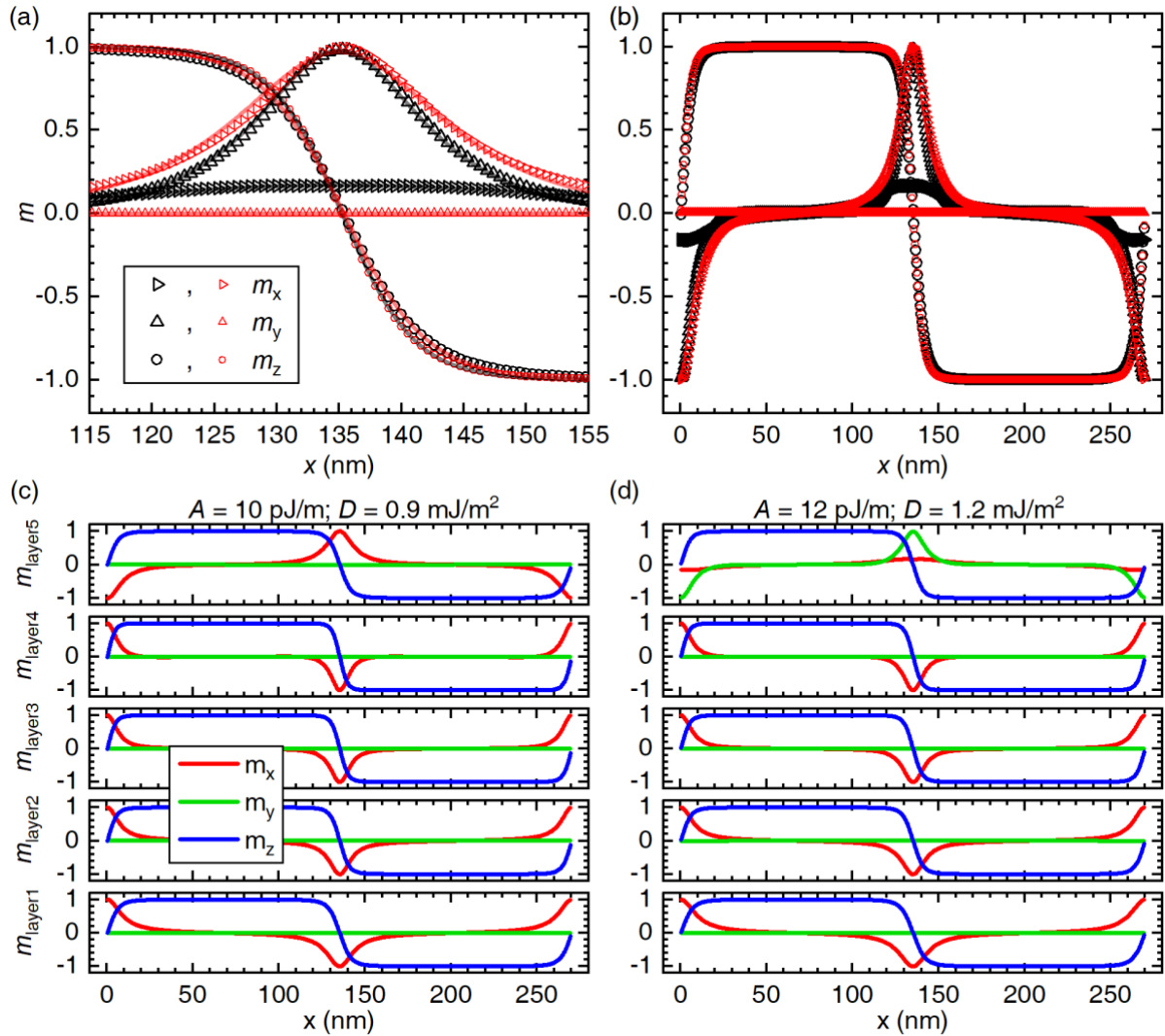


Figure S3: Magnetization profile of the minimized domain walls of the studied multilayer. (a) Detailed magnetization profile of the top magnetic layer (layer 5) of the sample. The black (red) symbols correspond to $A = 10$ pJ/m ($A = 12$ pJ/m) and $D = 0.9$ mJ/m² ($D = 1.2$ mJ/m²). This panel displays only the central domain wall area. Lines are fit (in the displayed range) using the formula of Sec. S5. (b) Same as in (a) but displaying the complete period. (c-d) Magnetization profile in each layer of the simulated multilayer for the set of parameters indicated on top of the graphs, corresponding to the circles in Fig. S2. Layer 1 is in contact with the buffer/substrate, while layer 5 is the top one, mostly probed by x-rays.

S2. On the influence of FEL intensity on measured dichroism

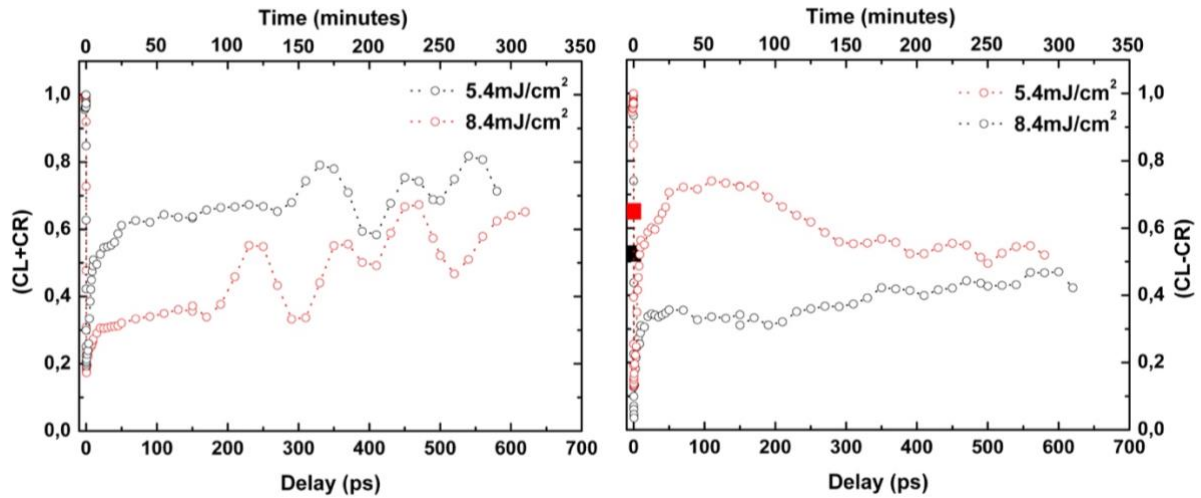


Figure S4. Left: Time dependence of the sum $(CL+CR)$ magnetic intensity for two fluences of the IR laser representing the main magnetization. Right: The corresponding time dependence of the dichroism $(CL-CR)$ that is related to both the magnetic moment and the magnetic chirality.

At the beginning of our experiment we started to perform delay scans for different IR laser fluence and with the full XFEL fluence of ~ 1.1 mJ/cm². In Fig. S4, we report both $(CL+CR)$ and $(CL-CR)$ signals, normalized to one for negative time delay, measured for 5.4 and 8.4 mJ/cm² IR fluence, which are typical for ultrafast demagnetization studies [23]. Between two delay scans, we moved to a fresh part of the sample. Looking first to $(CL+CR)$, one can notice the ultrafast decrease of magnetization in the first 500 fs, followed by a relaxation time that increase with the pump laser fluence. A second feature that we can notice is the pronounced and well-defined oscillation with a characteristic timescale of around 160 ps (~ 6 GHz) that is discussed in the main text of the paper. Focusing now on the dichroism $(CL-CR)$ time dependence, we observe after an ultrafast decrease a beginning of recovery. The dichroism stays almost constant for the strongest fluence (7.5 mJ/cm²) and start to recover for 4.8 mJ/cm² but then drops slowly back to a smaller value close to 40% of its initial value. We can see that for strong IR fluence and full XFEL the $(CL-CR)$ never recovers (big black square) and stays almost at the same value reached at the end of the delay scans. For a lower IR fluence, still with full XFEL, we can observe a dichroism $(CL-CR)$ that only partly recovers when going to negative delays (big red square in Fig. S2). This intriguing behavior of the dichroism, although the magnetization behaves as reported in previous work [22, 25], is not to be attributed to an ultrafast phenomenon but is related to the long exposure of the sample to both IR and FEL beam during this scan that takes 2 hours as shown in the top legend of Fig. S2. After some further experiments, we can confirm that this behavior was due to the FEL intensity that we have to attenuate by $\sim 50\%$ to recover an artifact-free result as in Figs. 3 and 4 of the main text. Unlike the IR laser beam, the main part of the 60 eV FEL intensity is absorbed by the first Pt/Co/Al period of our multilayers. During long and repeated exposure of the x-ray beam, the sample interfaces might slightly change (intermixing), inducing a change of the DMI amplitude and consequently a reduction of the measured dichroism. This must be checked by measuring again the initial state of the sample with going to negative delay (1 ps) measured after the complete time dependence.

S3. Data Analysis

We record the scattering diagram with a PI-MTE CCD camera (2040x2048 pixels, 13.5 μ m in size each) from Princeton Instruments located at 12 cm from the sample. For each delay between the IR laser and the XFEL pulses we recorded 500 shots per CCD picture and stored them in an HDF5 file containing also the experiment contextual data (x-ray wavelength, FEL single shot intensity, FEL single shot spectral content, ...). In order to reduce the reading time, the images have been binned 2x2. In order to renormalize by the bunch intensity, an I-zero has been measured by recording the intensity of a

4 quadrants photodiode placed at the entrance of the experimental end-station measuring the tail of the beam for each bunch. Assuming that the spatial position variation from shot to shot is small compared to the photodiode size, as it can be expected at seeded FEL as FERMI, this I0 value is proportional to the incident intensity and can be used to normalize the count on each CCD image.

For each delay we accumulate 500 images and sum them in order to obtain the raw data shown in Fig. 1. Using these values, to avoid any artifact, we chose to remove all the x-ray bunches that differ by 20% from the average bunch intensity. This procedure allows us to remove, e.g., all the images where the FEL intensity was zero, or too intense to be representative. In total, more than 20% of the total data were removed from the image list during a time resolved scan. Then, each image is normalized by its corresponding I-zero intensity. The images are then sorted by time delays and FEL polarization. Files with the same delay and polarization are averaged. Additional information is extracted, such as the FEL wavelength, incident angle and the CCD to sample distance, which is used to convert geometric related distance into sample characteristic properties later on. Before and after each delay scan, multiple CCD background images were performed in order to account for the CCD's electrical noise. The averaged background image is subtracted from the measurement images.

Final images are sorted by time delay and separated by polarization, i.e., circular left and right. For each delay, the two images are resized by a geometric factor to account for the 45° incident angle. The final sum (CL + CR), difference (CL – CR), and the asymmetry ratio (CL – CR)/(CL + CR) images are then calculated. Since the FEL spot slightly moves while changing polarization, one obtains erratic points at the edge of the beamstop which affects the data analysis. Both, polar and radial masks are applied on the images to totally hide the beamstop, which consists on replacing pixel values within the range of the mask by zeros as it can also be seen in Fig. 1. We then extract the center of the scattering pattern as the center of the diffraction ring in the sum image. Thereafter we perform a radial profile on the three images. The radial profile excludes zero values outside of the beamstop radius in order to keep the full radius range of the image in the chart and to make a radial normalization by non-zero values only.

In order to remove the diffuse scattering peaking at the specular position, a large disk around the specular position is excluded from the analysis. This is particularly important for the (CL+CR) images and has a negligible influence on the dichroism (CL-CR). The diffuse scattering background is fitted using a third order polynomial function using the intervals between diffraction peaks indicated by the vertical green dotted lines in Fig. S5.

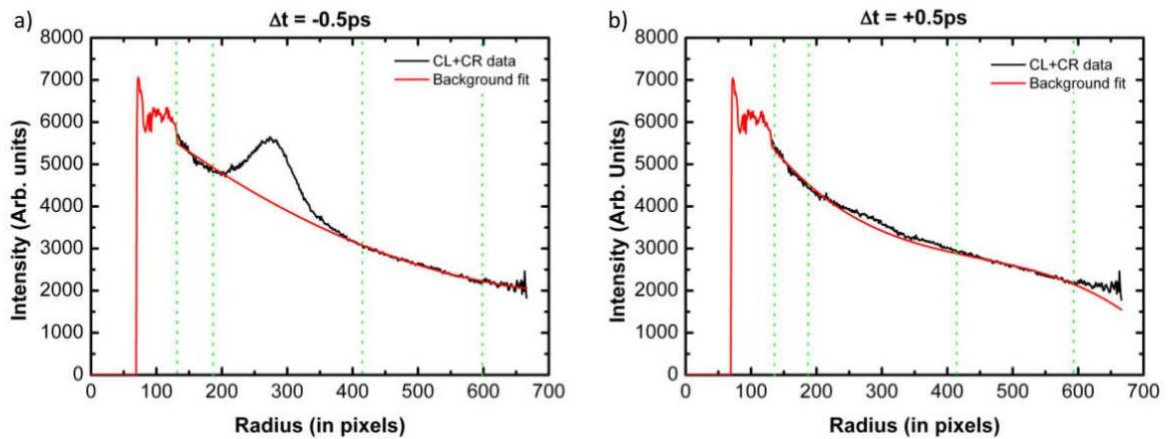


Figure S5: Typical rRadial profile of the sum image (black) for delay times of -0.5 ps (a) and 0.5 ps (b) fit with a cubic function (green line).

After removing this background, the diffraction ring peak is fitted by a Gaussian. From the Gaussian fit we can directly extract the values used in the manuscript as the full width at height maximum (FWHM) and the position of the peaks in wave vector (μm^{-1}). We check in Fig.S6 that the numerical integration of the peaks matches perfectly the areas of the Gaussian fitted functions.

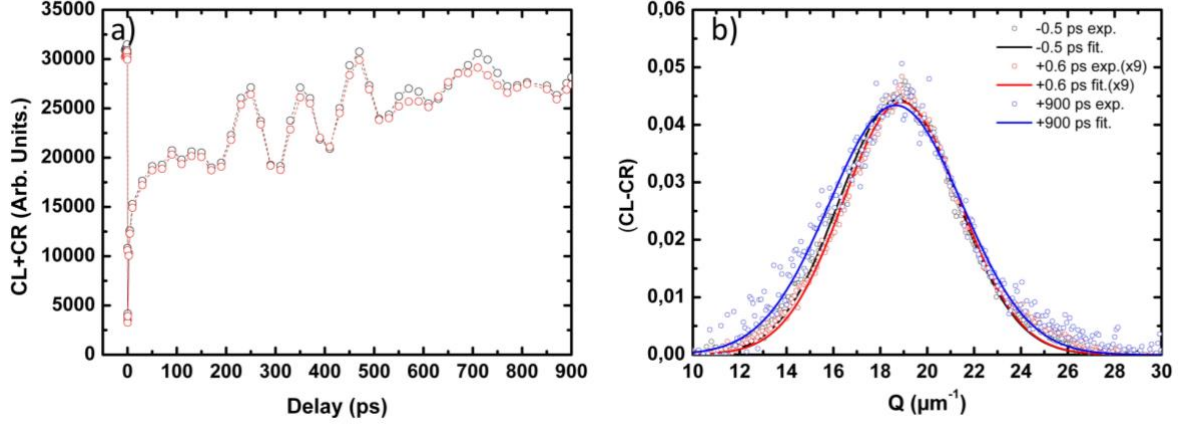


Figure S6: a) Integration of the (CL+CR) magnetic peak (black) and its integral from the gaussian fit (red). b) Fit by a gaussian function of (CL-CR) magnetic peaks before pumping (-0.5 ps), at the maximum of demagnetization (+0.6 ps) and at long timescale (900 ps).

S4. Time dependence analysis

The characteristic timescale for demagnetization and recovery is obtained by fitting (CL+CR) and (CL-CR) over the full timescale as shown in inset of Fig. 4(c). However, we also fitted the first few ps to be more accurate on the ultrafast timescale and the results are shown in Fig. 2(a). The time constant given in the main text is extracted from the (CL+CR) and (CL-CR) data fit by the equation in Ref. [24]:

$$\frac{I(t)}{I_0} = \{a - [-b \cdot e^{-t/t_1} + c \cdot e^{-t/t_2} + d \cdot e^{-t/t_3}] \Theta(t)\} \otimes \Gamma(t), \quad (S1)$$

where t_1 is the demagnetization time, t_2 and t_3 are the recovery times. The Θ function is the Heaviside function, which is convoluted by Γ , a Gaussian function with 120 fs full width at half maximum (FWHM) approximating the experimental temporal resolution blur due to the finite FEL and IR laser pulse width. The FWHM of Γ corresponds to the mean squared duration of the XUV and IR pulses of 60 and 100 fs, respectively. For the demagnetization constant timescale, we obtain 150 ± 30 fs for both the dichroism (CL-CR) and the sum (CL+CR). Both values are the same within the error bars of the fit, and it is probably limited by our experimental time resolution of 120 fs. For the recovery where we found time constants of the fast recovery of 4 ± 0.5 ps for (CL-CR) (6.5 ± 1 ps for (CL+CR)) and a slow recovery time of 290 ± 20 ps for (CL-CR) (600 ± 30 ps for (CL+CR)). From this crude analysis, one sees that the two quantities, sum and dichroism, have different recovery time scales.

S5. Simulation of Asymmetry Ratio with a transient mixed Bloch/Neel/Bloch wall

The profile of a 1D mixed Bloch/Neel/Bloch is modelled as followed:

$$M_x(x, t) = \cos(\Theta(t)) M(t) \left[\sqrt{1 - \left(\tanh \left(\lambda \frac{x_1(x)}{w(t)} \right) \right)^2} - \sqrt{1 - \left(\tanh \left(\lambda \frac{x_2(x)}{w(t)} \right) \right)^2} \right]$$

$$M_y(x, t) = \sin(\Theta(t)) M(t) \left[\sqrt{1 - \tanh \left(\tanh \left(\lambda \frac{x_1(x)}{w(t)} \right) \right)^2} - \sqrt{1 - \tanh \left(\tanh \left(\lambda \frac{x_2(x)}{w(t)} \right) \right)^2} \right]$$

$$M_z(x, t) = \sin(\Theta(t)) * M(t) * \left[\sqrt{1 - \tanh \left(\left(D * \frac{x_1(x)}{w(t)/2} \right) \right)^2} - \sqrt{1 - \tanh \left(\left(D * \frac{x_2(x)}{w(t)/2} \right) \right)^2} \right]$$

$$M_x(x, t) = \cos(\Theta(t)) * M(t) * \sqrt{1 - \tanh\left(\left(D * \frac{x_1(x)}{w(t)/2}\right)^2\right)} - \sqrt{1 - \tanh\left(\left(D * \frac{x_2(x)}{w(t)/2}\right)^2\right)}$$

$$M_z(x, t) = M(t) \tanh\left(\frac{D\lambda}{2} * \frac{x_3}{w(t)}\right)$$

With $x_1(x) = \sin\left(\pi \frac{x + \frac{D\lambda}{2}}{2 * D\lambda} - \frac{\pi}{4}\right)$, $x_2(x) = \sin\left(\pi \frac{x + \frac{D\lambda}{2}}{2 * D\lambda} + \frac{\pi}{4}\right)$ and $x_3(x) = \sin\left(2\pi \frac{x}{D\lambda}\right)$, x is the position and λ the period of the domains (twice the domain size). Both are in nanometer as shown in Fig. S5(a). $\Theta(t)$ is the tilt angle arising from the torque impose by hot electrons, $w(t)$ corresponds to the time evolution of the DW width, and $M(t)$ is the temporal evolution of magnetization and is proportional to $\sqrt{(CL + CR)}$.

We display in Fig. S5(a) the result for the magnetization profile for $\Theta = 0^\circ$ and $\Theta = 40^\circ$. We calculate the scattering intensity using the resonant scattering amplitude in dipolar approximation using [S4, S5, S6], without considering the charge scattering:

$$f_{EI}^{REXS} = \begin{pmatrix} 0 & \mathbf{k} \\ -\mathbf{k}' & \mathbf{k}' \times \mathbf{k} \end{pmatrix} \cdot \mathbf{M} .$$

The diffracted intensity for a given incident polarization is expressed as follows [S5]:

$$I = Tr[\tilde{f}\rho\tilde{f}^\dagger],$$

where \tilde{f} and \tilde{f}^\dagger are the Fourier transform of the scattering amplitude f_{EI}^{REXS} and its complex conjugate, respectively, and ρ is the density matrix of the incident x-ray beam. In the Stoke-Poincaré representation [S5], the density matrix for a circularly left or right incident beam is expressed as follows:

$$\rho_{CL} = \frac{1}{2} \begin{pmatrix} 1 & -i \\ i & 1 \end{pmatrix} \text{ and } \rho_{CR} = \frac{1}{2} \begin{pmatrix} 1 & i \\ -i & 1 \end{pmatrix}$$

In Fig. S7(b) we represent the simulated asymmetry ratio for the several scenarii discussed in the main text. The results are normalized by the ratio simulated for a DW width of 22 nm and a 0° wiggling angle Θ corresponding to the static parameters issued from micromagnetic simulations (See S1 for details). The lowest value of the experimental ratio can be simulated in each model, i.e, keeping the DW magnetization equal to the domain ones, or with a reduction of the magnetization within the DW proportional to $\cos(\Theta)$, $\cos^2(\Theta)$ or to $1 - \sin(\Theta)$.

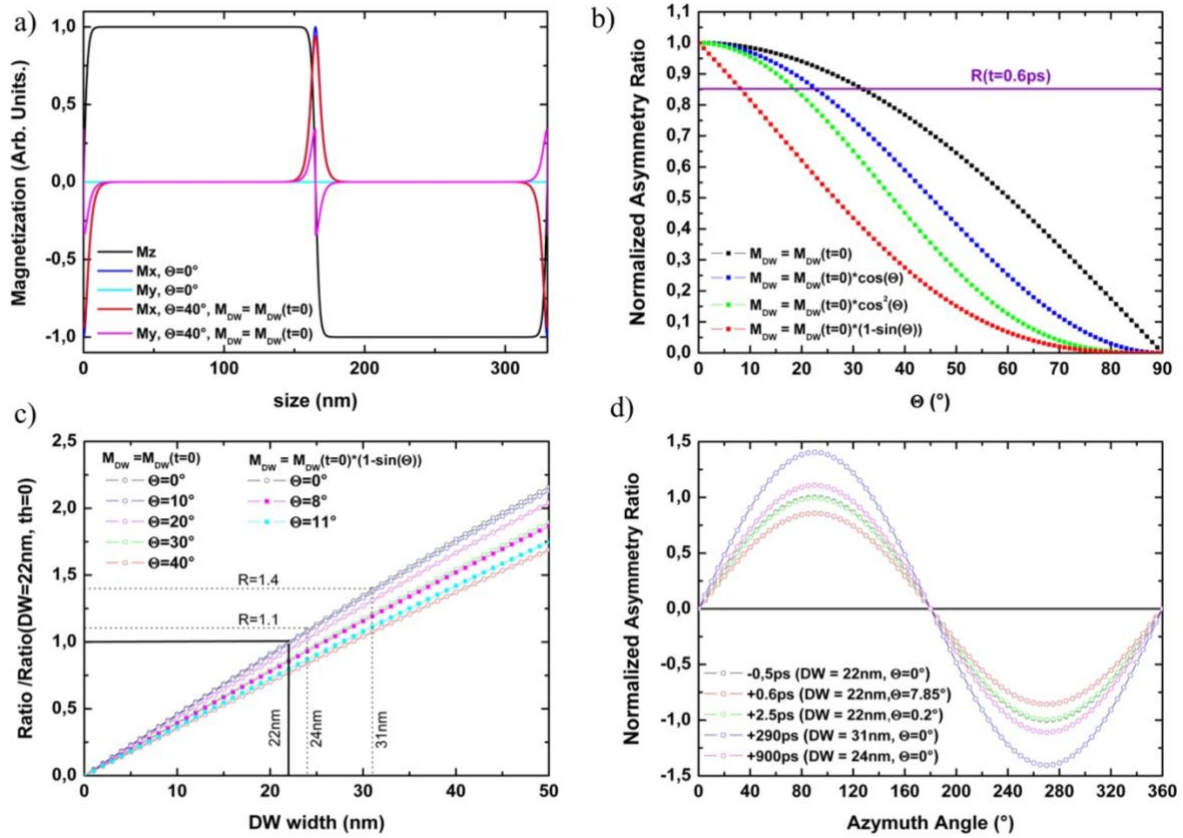


Figure S7. a) Representation of the magnetization for $\Theta=0^\circ$ and 40° . b) Simulation of the asymmetry ratio $(CL-CR)/(CL+CR)$ for different delays. The parameters used for the simulations are in the legend. d) Simulation of the asymmetry ratio function of the DW size for different Θ .

We also simulate the evolution of the magnetic asymmetry ratio as a function of the DW width for a magnetization in the DW equal to the one in domain or reduced. It shows that to account for the maximum asymmetry ratio of 1.4 observed at long timescales, one has to account for a dilatation of the DW from 22 nm up to 31 nm. Lastly, in figure S7(d) we represent the simulated orthoradial profiles with a DW magnetization proportional to $1 - \sin(\Theta)$.

S6. Analysis of the orthoradial distribution of dichroism in x-ray resonant scattering

We explore the possible evolutions and change of the type of chirality during the first few ps performing orthoradial integration of the $(CL-CR)$ images at several characteristic delays after having first determined the center of the diffraction ring. Finally, the background contributions is minimized by integrating the ring intensity where it is about two orders of magnitude larger than the background, only in the range defined by the two red circles shown in Fig. S6(a).

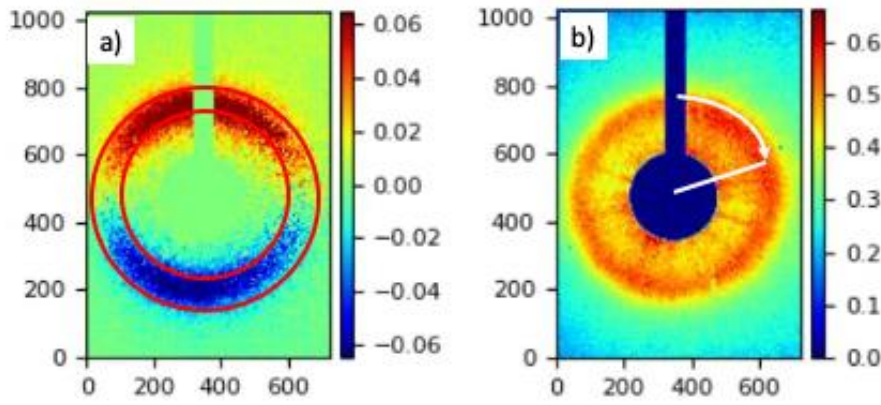


Figure S8. (a) (CL-CR) with in red the two circles defining the zone for radial integration. (b) Corresponding (CL+CR) image.

The result of the radial integration is shown in Fig. S9. The azimuth angle is defined as shown in Fig. S8(b). We choose several characteristic delays starting from -1 ps. The 0.6 ps is the delay for the maximum of demagnetization while 2.6 ps is representative to the expansion of the DW width. We also display 50 ps and the last measured delay at 900 ps representative of the long timescale behavior, where the initial CR-XRMS is completely recovered.

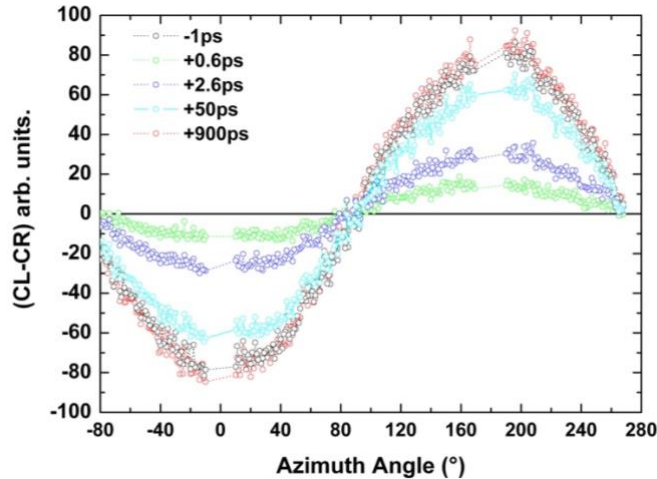


Figure S9: Orthoradial dichroic profiles for different delays. The beamstop mask correspond to 0° and 180° .

In our experiment all curves merge at 90° without any measurable shift, indicating that during all the demagnetization even at ultrafast timescale the DMI remain preset and impose the type of magnetic texture (Néel in this sample) and its chirality. We would like to point out that this orthoradial profile is fully compatible with the proposed scenario of a transient mixed Bloch/Néel/Bloch domain wall suggested to explain the ultrafast timescale deviation from one of the asymmetry ratio.

S7. Tr-MOKE

Time-resolved magneto-optical (tr-MOKE) measurements have been carried out in order to investigate magnetization dynamics when our Pt/Co/Al multilayer is fully saturated. Indeed, while we probed the periodically ordered magnetic state using time-resolved XRMS, in the case of the tr-MOKE measurements, an out-of-plane magnetic field ($\mu_0 H = \pm 0.2$ T) is applied to uniformly saturate the Pt/Co/Al multilayer.

In this setup, ultrafast magnetization dynamics is assessed in a pump-probe scheme. An amplified Ti:Sapphire laser provides 800 nm light pulses at 1 kHz to pump the magnetic multilayer. A small fraction of the main beam is picked up and frequency-doubled through a Beta Barium Borate crystal into a 400 nm laser pulse. Pulse durations of both pump and probe pulses are about 100 fs. While the pump beam is collimated and perpendicular to the sample surface, the probe is focused on the sample

surface to a 10 μm diameter beam with a 45° angle with respect to the pump (inset of Fig S10). In the magneto-optical Kerr effect, the polarization state of the light, after being reflected on a magnetic surface, depends on the magnetization amplitude and direction. Therefore, any change of magnetization properties is translated into a change of polarization state of the reflected beam. The time-resolved change of polarization of the reflected probe (rotation in our case) is analyzed using a set of half-lambda waveplates, Wollaston prism, and balanced photodetector.

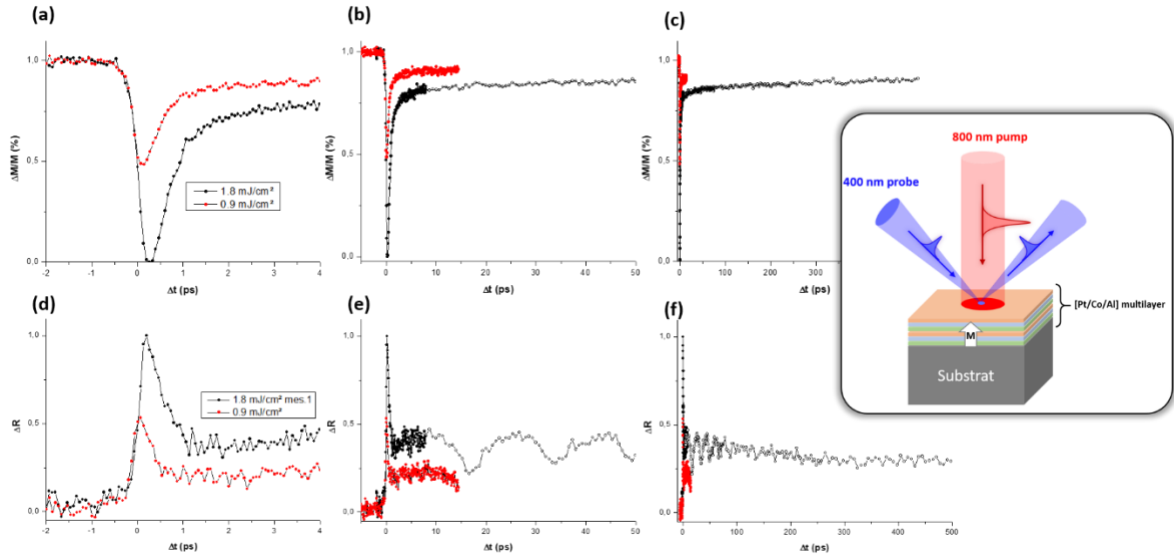


Figure S10: Time-resolved magneto-optical measurements. (a-c) ultrafast magnetization dynamics assessment. (d-f) measurement of the ultrafast change of reflectivity. Note that all curves are normalized.

Figure S10 presents the time-resolved magneto-optical measurements performed on the Pt/Co/Al multilayer. Regarding magnetization dynamics (Fig. S10(a-c)), within our time resolution, we observe a typical ultrafast dynamical behavior as already reported in various studies, that is to say, a fast quench of the magnetic moment in some hundreds of fs, followed by a fast and a slower re-magnetization. Yet no oscillation can be observed. This corroborates the fact that the observed oscillations in the time-resolved XRMS measurements are related to the domains/domain-walls striped order. Noteworthy, in order to separate magnetization dynamics from transient optical dynamics, the presented graphs (Fig. S10(a-c)) result from the difference between measurement at (+ H) and (- H). On the other hand, time-resolved changes of reflectivity can be simultaneously assessed (Fig. S10(d-f)). After a short peak at the ultrashort timescale related to the ultrafast photoinduced generation of hot carriers, oscillations of the time-resolved reflectivity signals are visible with a main frequency at about 60 GHz and certainly a beating at 3-3.5 GHz. The oscillations can be ascribed to acoustic modes, triggered (and probed) in the topmost portion of the metallic multilayer and escaping into the Si substrate, the frequencies of which are calculated as described in Sec. S9.

S8. VNA-FMR

Broadband vector network analyzer ferromagnetic resonance (VNA-FMR) measurements were carried out to probe the power absorbed from a radio-frequency (rf) magnetic field as a function of the rf frequency in the presence of an additional bias field. Figure S11 shows the change in rf power absorbed by the sample, which was determined from the differential of the rf transmission, S_{21} , with respect to field. The signal is weak and the results shown are obtained from an average of 10 frequency-field maps.

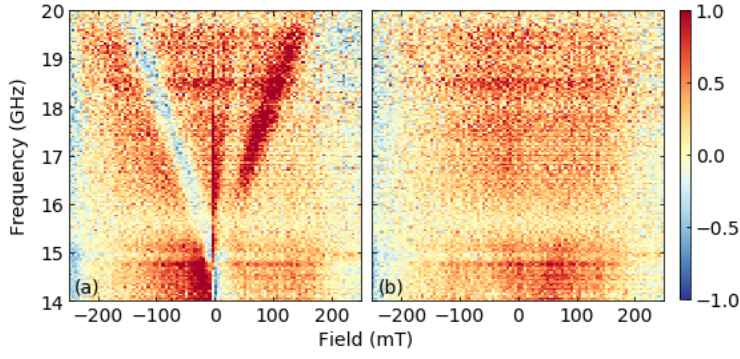


Figure S11: VNA-FMR measurement. with bias field applied (a) out-of-plane and (b) in-plane of the sample.

The figure shows VNA-FMR measurements with the bias field applied (a) out-of-plane and (b) in-plane of the sample. In both cases, the rf field is applied in-plane and perpendicular to the bias field. No features could be observed below 15 GHz (not shown). Features, which occur only for the out-of-plane field at frequencies >15 GHz, correspond to the FMR uniform precession. The value at zero field allows the effective anisotropy to be precisely estimated (see Section S1).

S9. Frequencies of acoustic and magnetic modes

S9.I. Frequencies of acoustic modes

The optical pump pulse generates transient elastic strain near the surface of the multilayer stack Si | SiO₂ | Ta (5) | Pt (8) | [Co (1.5) | Al (1.4) | Pt (3)] ×4 | Co (1.5) | Al (1.5) (thicknesses in nm). The strain pulse propagates from the surface into the inner part of the stack, experiencing multiple reflections from the interlayer interfaces and outer surfaces. These reflections lead to proliferation of strain pulses bouncing back and forth between various interfaces. The interference between these pulses leads to formation of standing waves. Their characteristic frequencies, which may be present in the time-resolved signals measured from the topmost part of the sample, are determined by the times of the pulse round trips across the individual layers or sets of those and by additional phase shifts that may be produced by reflections. The strongest wave amplitude is expected for confinement between interfaces causing the strongest reflections. The strength of a reflection from an interface increases as the mismatch of the acoustic impedances of the adjacent layers increases.

Table S1. Properties of the stack's constituent layers.

	K (GPa)	G (GPa)	ρ (kg m ⁻³)	c_l (km s ⁻¹)	c_t (km s ⁻¹)	Z_l (MPa s m ⁻¹)	Z_t (MPa s m ⁻¹)
Co	153	83	8800	5.5	3.1	48	27
Pt	236	62	21500	3.8	1.7	83	37
Al	81	25	2700	6.5	3.0	18	8
Ta	204	69	16700	4.2	2.0	70	34
Si	37	80	2300	7.9	5.9	18	14
SiO ₂	40	28	2200	5.9	3.6	13	8

Table S1 summarizes the values of the bulk modulus, K , the shear modulus, G , and the density, ρ , of the stack's constituent layers, together with the corresponding values of the speed of longitudinal, $c_l = \sqrt{\left(K + \frac{4}{3}G\right)/\rho}$, and transverse, $c_t = \sqrt{G/\rho}$, sound and those of the longitudinal, $Z_l = \rho c_l$, and transverse, $Z_t = \rho c_t$, acoustic impedances. The strongest impedance mismatch occurs at the $\text{SiO}_2 | \text{Ta}$ interface. This promotes formation of a standing wave across the metallic stack with a total thickness of $L = 39.6$ nm. Due to the impedance of the substrate being lower than that of the metallic stack, the wave's wavelength is equal to $2L$, while its frequency is equal to the inverse of the round-trip time of the acoustic pulse. Table S2 presents the wave's frequencies for speeds of the order of those shown in Table S1. The frequencies corresponding to sound speed values characteristic for longitudinal phonons in the sample have a similar magnitude to the 60 GHz value observed experimentally in tr-MOKE experiment. This is consistent with the fact that optical pump pulses cannot couple to transverse phonons in our experimental geometry, in which the optical spot size is greater than the film thickness by orders of magnitude.

Table S2. Estimates of the standing wave frequency for different values of the speed of sound.

Speed of sound (km s^{-1})	2	3	4	5	6
Frequency (GHz)	25	38	50	63	76

These considerations can be put on a more rigorous footing by calculating the spectral response of a one-dimensional stack of elastic materials to a time-periodic force source at its outer surface. The real part of the velocity response is then peaked at the resonant frequencies of the structure. The response can be easily found by solving the one-dimensional wave equation, for which we employed a custom-made simulation. Fig. S12 shows the result of this calculation for the surface of a structure with properties described in Table S1 and subjected to a longitudinal force, i.e. acting normal to the film plane. The response exhibits several resonant peaks. The finite widths of the peaks, of about 4-5GHz, are due to the sound escaping from the stack into the semi-infinite space representing the substrate. The three lowest resonant frequencies are 48.6 GHz, 104.9 GHz, and 155.8 GHz, respectively. This further confirms the identification of the 60 GHz contribution to the reflectivity signal (Fig. 10(d-f)) as an acoustic mode.

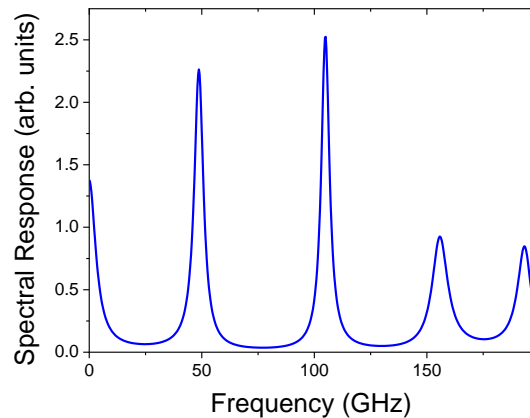


Figure S12: The calculated longitudinal acoustic spectral response of the studied sample.

S9.II. Frequencies of magnetic modes

The magnetic layers in the stack have a strong out-of-plane anisotropy and form a multi-domain state at zero bias magnetic field. The nonuniformity of the magnetization associated with the magnetic domains can mediate excitation of magnetic precessional modes even by uniform stimuli, such as the optically induced transient heating and/or elastic strain. The lowest precessional frequency associated with the magnetic domains (rather than domain walls) can be estimated as

$$f = \gamma\mu_0(H_A - H_d + H_{\text{ex}}), \quad (\text{S2})$$

where $\gamma = 28$ GHz/T is the gyromagnetic ratio, μ_0 is the permeability, H_A is the out-of-plane anisotropy field, H_d is the demagnetizing field, and H_{ex} is the exchange field.

From the measurement of the in-plane saturation field, we estimate $\mu_0(H_A - H_d) \cong 0.55$ T. This corresponds to a uniform ferromagnetic resonance (FMR) mode frequency of our sample (in the uniform state and zero bias magnetic field) of $\gamma\mu_0(H_A - H_d) \cong 15.4$ GHz.

The exchange contribution to the frequency originates from the nonuniformity associated with formation of a standing spin wave across each stripe domain, i.e., $\gamma\mu_0 H_{\text{ex}} = 2\gamma A k^2 / M_s$, where k is the wave's wave number, A is the exchange constant, and M_s is the saturation magnetization. The wavelength λ of the spin wave can be estimated as twice the domain size. Then, for $\lambda \cong 400$ nm, $A = 12$ pJ/m, and $M_s = 1069$ kA/m, we obtain $\gamma\mu_0 H_{\text{ex}} \cong 0.1$ GHz. Any contribution from the Dzyaloshinskii–Moriya interaction should be even smaller than this.

Using Eq. (S2), we obtain for the lowest precessional frequency associated with the magnetic domains $f \cong 15.5$ GHz. Experimentally observed frequencies smaller than this must therefore be assigned to magnetic modes associated with the domain walls.

References:

- [S1] Exl L. et al., J. Appl. Phys. 115, 17D118 (2014).
- [S2] Mulkers et al., Phys. Rev. B 95, 144401 (2017)
- [S3] F. Ajejas et al., in preparation.
- [S4] J. P. Hannon, et al., Phys. Rev. Lett. 61, 1245 (1988).
- [S5] J. P. Hill and D. F. McMorrow, Acta Crystallogr. Sect. A 52, 236 (1996).
- [S6] G. van der Laan, C.R. Phys. 9, 570 (2008).